

Epitaxial stabilization of pulsed laser deposited $\text{Sr}_{n+1}\text{Ir}_n\text{O}_{3n+1}$ thin films: entangled effect of growth dynamics and strain

Araceli Gutiérrez-Llorente,^{1,*} Lucía Iglesias,² Benito Rodríguez-González,³ and Francisco Rivadulla²

¹*Universidad Rey Juan Carlos, Escuela Superior de Ciencias Experimentales y Tecnología, Madrid 28933, Spain*

²*Centro Singular de Investigación en Química Biolóxica e Materiais Moleculares (CiQUS),*

Departamento de Química-Física, Universidade de Santiago de Compostela. 17582 Santiago de Compostela (Spain)

³*Departamento de Química Física, Universidad de Vigo, 36310 Vigo, Spain*

The subtle balance of electronic correlations, crystal field splitting and spin-orbit coupling in layered Ir^{4+} oxides can give rise to novel electronic and magnetic phases. Experimental progress in this field relies on the synthesis of epitaxial films of these oxides. However, the growth of layered iridates with excellent structural quality is a great experimental challenge. Here we selectively grow high quality single-phase films of Sr_2IrO_4 , $\text{Sr}_3\text{Ir}_2\text{O}_7$ and SrIrO_3 on various substrates from a single $\text{Sr}_3\text{Ir}_2\text{O}_7$ PLD target by tuning background oxygen pressure and epitaxial strain. We demonstrate a complex interplay between growth dynamics and strain during PLD growth. Such interplay leads to the stabilization of different phases in films grown on different substrates under identical growth conditions, in contrast with a simple kinetic model. We further investigate the thermoelectric properties of the three phases and propose that weak localization is responsible for the low temperature activated resistivity observed in SrIrO_3 under compressive strain.

I. INTRODUCTION

Transition-metal oxides with partially filled d -electron states exhibit exceptionally rich electronic and magnetic phase diagrams.^{1–3} Strong Coulomb interactions in narrow $3d$ -bands can lead to Mott insulators ground states. Moving down into $5d$ transition metal ions, the spatial extent of the orbitals increases, resulting in a stronger $5d$ - $\text{O}:2p$ overlap. This widens the electronic bands, thus reducing electronic correlations, whereas the contribution of the crystal-field energy, Δ , increases. Moreover, the higher atomic number results in a significant contribution of the spin-orbit coupling (SOC) energy. As a result, $5d$ -Iridium (Ir^{4+}) oxides constitute a family of materials in which SOC, Δ and electronic correlations present a comparable magnitude. Within this context, it has been proposed that SOC splits the threefold degenerate t_{2g} band in Sr_2IrO_4 into a lower $J_{\text{eff}}=3/2$ band, and a half-filled $J_{\text{eff}}=1/2$ band. Coulomb interactions or additional structural distortions introduce further splitting in that narrow $J_{\text{eff}}=1/2$ band, opening up a charge gap, which can be manipulated by epitaxial strain.^{4–13}

The Ruddlesden-Popper (RP) series of strontium iridates, $\text{Sr}_{n+1}\text{Ir}_n\text{O}_{3n+1}$, features a Mott-metal crossover from that insulating ground state of Sr_2IrO_4 (with a two dimensional IrO_6 corner-sharing octahedral network characteristic of $n = 1$) to a correlated metallic state in the three dimensional perovskite SrIrO_3 ($n = \infty$).¹⁴ This suggests the possibility of fine-tuning the charge gap across $\text{Sr}_{n+1}\text{Ir}_n\text{O}_{3n+1}$ by growing high quality epitaxially strained thin films. Theoretically, tensile strain brings about an increase of the Ir-O-Ir bond angle that could favour larger bandwidths and conductivity, at least for $n = 1$.¹¹ In such case, Serrao et al.¹² proposed that the charge gap in Sr_2IrO_4 depends on the ratio c/a of lattice parameters. But, as n increases the hopping along the c -axis becomes more relevant, and thus such a simple

analysis might be no longer adequate for other members of the RP series.

From a technological point of view, the spin Hall effect arising from SOC in these materials lies at the heart of potential applications of antiferromagnetic Sr_2IrO_4 and $\text{Sr}_3\text{Ir}_2\text{O}_7$ in spintronic devices. Notable achievements in this field are the detection of anisotropic magnetoresistance in Sr_2IrO_4 ,^{15–17} that could keep track of the antiferromagnetic order parameter; tunable transport properties of Sr_2IrO_4 and $\text{Sr}_3\text{Ir}_2\text{O}_7$ by applied electric fields;^{18,19} and bias induced resistive switching in $\text{Sr}_3\text{Ir}_2\text{O}_7$.²⁰

The experimental study of $\text{Sr}_{n+1}\text{Ir}_n\text{O}_{3n+1}$ calls for thin films single-phase crystalline materials, making indispensable a precise control of the growth process. As the unit cell of each member of the RP series is a superlattice that consists of ordered sequences of perovskite layers (SrIrO_3) sandwiched between two rock salt layers (SrO) along the c crystallographic axis, intergrowth of different members is frequently found.^{21,22} This renders the growth of such artificial layered phases a great experimental challenge, and their growth mechanisms, intriguing.^{23,24}

Off-stoichiometric transfer of material from a multi-component oxide target to the substrate in pulsed laser deposition (PLD) is an undeniable fact.^{22,25,26} It is widely accepted that the angular distribution of the species attaining the substrate is modified as a result of the atomic collisions between the atoms of the plume and the molecules of the gas,^{27,28} and changes in the oxygen background pressure can lead to a changeover in the growth mode.^{29,30} Furthermore, epitaxial strain has a major impact on growth dynamics as it modifies surface diffusion and mobility of adatoms, although the character of that shift is strongly material dependent, and has been little explored in oxides.^{30–34}

Here we report the selective growth of high quality single-phase films of Sr_2IrO_4 , $\text{Sr}_3\text{Ir}_2\text{O}_7$ and SrIrO_3 from

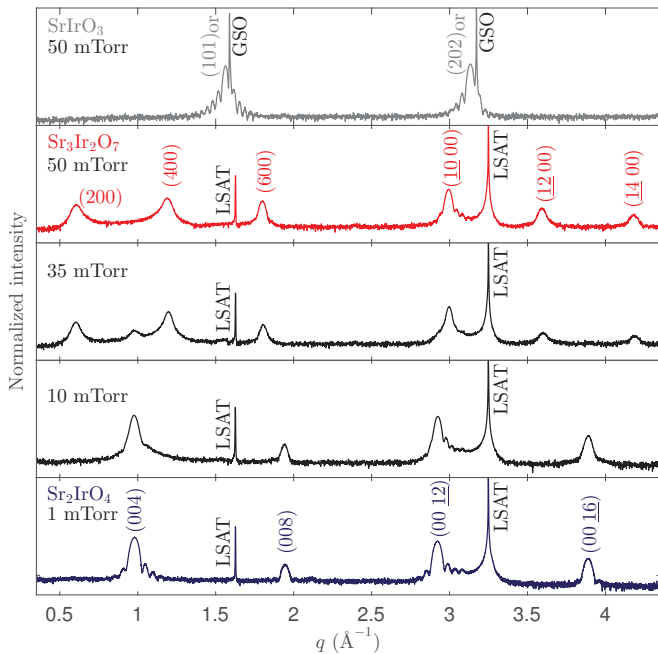


FIG. 1. Epitaxial synthesis of $n = 1, 2, \infty$ phases of $\text{Sr}_{n+1}\text{Ir}_n\text{O}_{3n+1}$ series from a single $\text{Sr}_3\text{Ir}_2\text{O}_7$ target. (a) Indexed XRD θ - 2θ scans of films grown on LSAT over an oxygen pressure range of 1 mTorr to 50 mTorr (from bottom to top), and on GSO at 50 mTorr (upper panel). Substrate temperature was 800 °C. As a rule, increasing the oxygen pressure promotes the stability of phases with larger n . The film grown at 35 mTorr on LSAT shows features that can be attributed to both $n=1$ and $n=2$ RP phases, suggesting a gradual transformation between the two phases. Noteworthy, $\text{Sr}_3\text{Ir}_2\text{O}_7/\text{LSAT}$ and $\text{SrIrO}_3/\text{GSO}$ are both grown on different substrates side by side in the PLD chamber. (see Fig. S1³⁵ for structural characterization of Sr_2IrO_4 and $\text{Sr}_3\text{Ir}_2\text{O}_7$ phases on STO substrates; Fig. S2³⁵ for θ - 2θ scans of $\text{SrIrO}_3/\text{GSO}$ films grown at oxygen pressure in the range 35 mTorr to 100 mTorr; and, Fig. S3 and Fig. S7³⁵ that provide evidence of the influence of substrate on the stabilization of RP phases in films grown under identical deposition conditions).

a single polycrystalline $\text{Sr}_3\text{Ir}_2\text{O}_7$ PLD target on substrates that impose different sign and degree of strain. The growth of films of these phases from a SrIrO_3 target on SrTiO_3 substrates has been achieved by Nishio *et al.*,³⁶ who focus on the thermodynamic aspects in the selective formation of these RP phases. Also, Liu *et al.*³⁷ have recently reported on the growth of Sr_2IrO_4 and SrIrO_3 films on SrTiO_3 substrates from a Sr_2IrO_4 target, featuring the critical role of oxygen partial pressure in the growth kinetics of the $\text{Sr}_{n+1}\text{Ir}_n\text{O}_{3n+1}$ epitaxial growth. Unlike previous works, we explore the impact of the strain imposed by the substrate on the growth of different phases. We demonstrate a complex interplay between strain and oxygen pressure during PLD growth that can lead to the stabilization of different RP phases in films grown on different substrates under identical deposition conditions of laser fluence, substrate temperature, and background

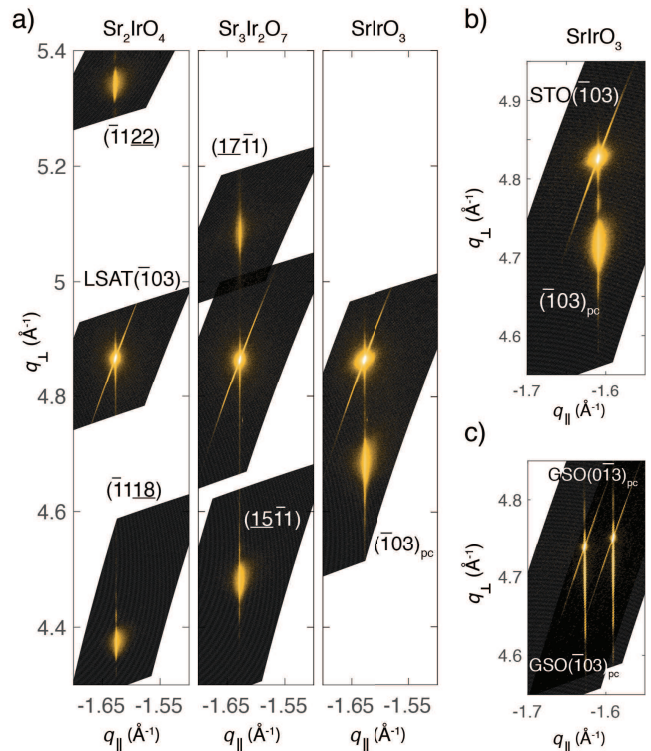


FIG. 2. a) High-resolution RSMs of Sr_2IrO_4 , $\text{Sr}_3\text{Ir}_2\text{O}_7$, and SrIrO_3 on LSAT. The $(\bar{1}03)$ reflection from the LSAT substrate is also shown in each map. b, c) RSMs around the $(\bar{1}03)$ substrate reflection for films grown on $\text{STO}(001)$ and $\text{GSO}(110)_{\text{or}}$, respectively. The pseudocubic reflections $(\bar{1}03)_{\text{pc}}$ and $(013)_{\text{pc}}$ in $\text{SrIrO}_3/\text{GSO}$ are observed at different $(q_{\parallel}, q_{\perp})$ (c). This is consistent with the deviation of β from 90° that takes account of the orthorhombic distortion in the perovskite.

oxygen pressure. We also discuss the effect of strain, oxygen pressure, and dimensionality on the temperature dependence of thermoelectric power, electrical resistivity, and magnetization of these materials.

II. RESULTS AND DISCUSSION

We grew 20 nm thick films of $\text{Sr}_{n+1}\text{Ir}_n\text{O}_{3n+1}$ with $n=1, 2$ and ∞ on $(001)\text{SrTiO}_3$ (STO), $(001)(\text{LaAlO}_3)_{0.3}(\text{Sr}_2\text{AlTaO}_6)_{0.7}$ (LSAT), and $(110)\text{GdSrO}_3$ (GSO) substrates by PLD from a single polycrystalline target of $\text{Sr}_3\text{Ir}_2\text{O}_7$. The laser fluence was optimized at $\approx 1 \text{ J/cm}^2$, and kept constant throughout the work. (See supplementary material for a detailed experimental description³⁵).

Fig. 1 shows x-ray diffraction (XRD) θ - 2θ scans of films grown on LSAT at an oxygen pressure of 1 mTorr, 10 mTorr, 35 mTorr and 50 mTorr, and on GSO at 50 mTorr, at a substrate temperature of 800 °C. The patterns of films grown at 1 mTorr and 50 mTorr on LSAT, and at 50 mTorr on GSO show all the peaks of Sr_2IrO_4 ,

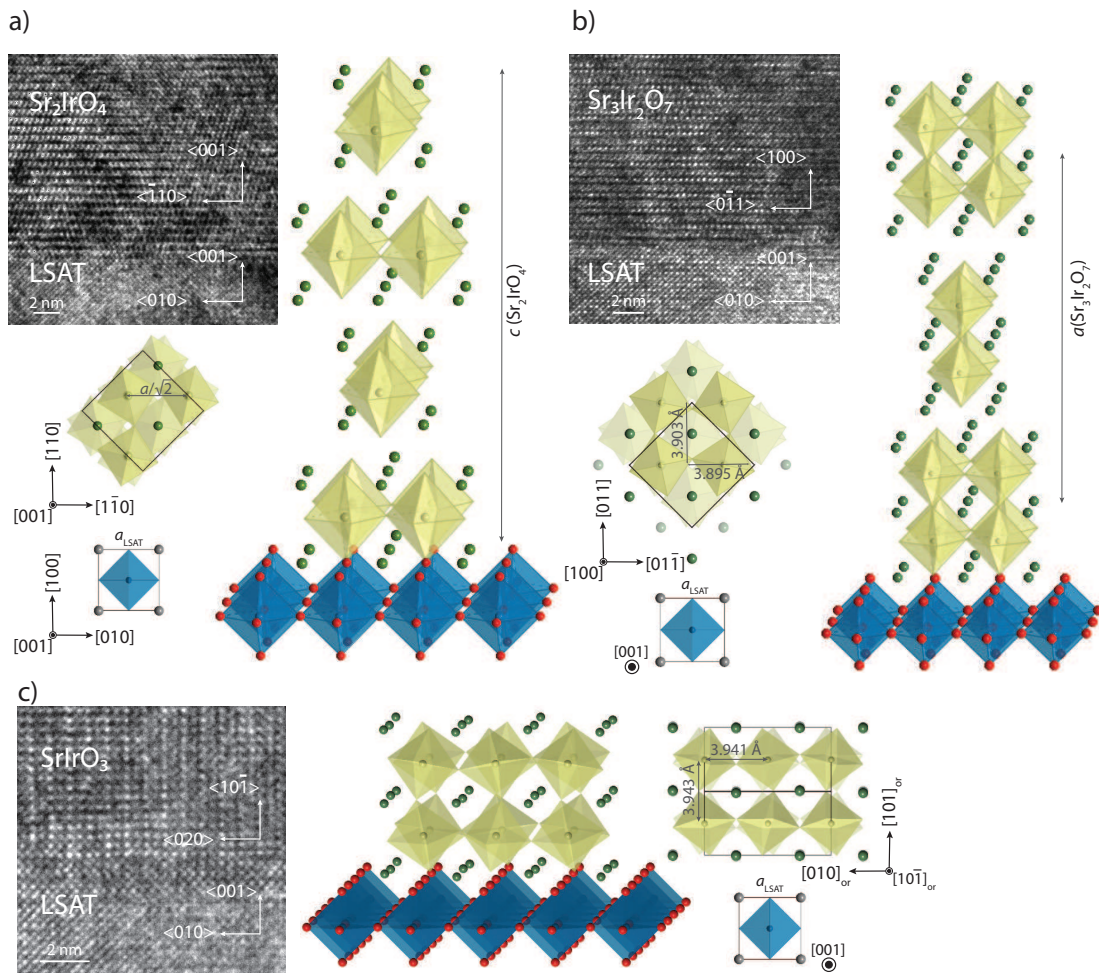


FIG. 3. High Resolution Transmission Electron Microscopy (HRTEM) images and structural model of the films on LSAT. Each panel shows the HRTEM image of the interface film/substrate, the 3D structural model, and the in-plane view. The deduced epitaxial alignments are outlined on each image. a) Tetragonal³⁸ $\text{Sr}_2\text{IrO}_4(001)\|\text{LSAT}(001)$, where the unit cell of Sr_2IrO_4 grows 45° rotated relative to the LSAT unit cell: $[110]\text{Sr}_2\text{IrO}_4\|[100]\text{LSAT}$. This enables lattice matching of $a(\text{Sr}_2\text{IrO}_4)/\sqrt{2} = 3.888 \text{ \AA}$ with $a(\text{LSAT})=3.868 \text{ \AA}$. b) $\text{Sr}_3\text{Ir}_2\text{O}_7(100)\|\text{LSAT}(001)$, where $\text{Sr}_3\text{Ir}_2\text{O}_7$ is depicted as a distorted perovskite (long axis along a ³⁹). This refined structure gives rise to an in-plane pseudocubic lattice of roughly 3.90 \AA . The unit cell of $\text{Sr}_3\text{Ir}_2\text{O}_7$ phase also grows 45° rotated relative to the LSAT substrate: $[011]\text{Sr}_3\text{Ir}_2\text{O}_7\|[100]\text{LSAT}$. c) Orthorhombic SrIrO_3 (b as long axis^{40,41}) shows an epitaxial relationship of $(10\bar{1})_{\text{or}}\|[101]_{\text{or}}\text{SrIrO}_3\|(001)[100]\text{LSAT}$. The tetrahedral rotation patterns expected for each space group in bulk are depicted. See Supplementary Information for electron diffraction patterns (Fig. S4³⁵).

$\text{Sr}_3\text{Ir}_2\text{O}_7$, and SrIrO_3 , respectively, oriented with the long axis along the substrate normal. There is no hint of impurity phases in these patterns which suggests that the sequence of perovskite and rocksalt layers are correctly ordered in the periodic structures along the out-of-plane direction (see discussion of Transmission Electron Microscopy data below). Strong Laue thickness fringes surrounding the main Bragg peak give evidence of an excellent structural quality of these films. The diffraction peaks of Sr_2IrO_4 can be indexed to the tetragonal unit cell: $a = 5.499 \text{ \AA}$ and $c = 25.784 \text{ \AA}$, space group $I4_1/acd$.³⁸ On the other hand, the peaks observed in $\text{Sr}_3\text{Ir}_2\text{O}_7$ are compatible with a subtly distorted perovskite described by a monoclinic space group ($C2/c$)³⁹ with parameters 20.935 \AA , 5.5185 \AA , and 5.5099 \AA , where the long cell

axis (a in the standard setting of space group $C2/c$) is parallel to the surface normal. In this structure, a single oblique angle $\beta=90.045^\circ$ produces a minute deviation from a quadratic lattice³⁹, which is below our X-ray experimental resolution. SrIrO_3 has been indexed to an orthorhombic perovskite cell with $Pnma$ symmetry and lattice parameters $a = 5.5909 \text{ \AA}$, $b = 7.8821 \text{ \AA}$, and $c = 5.5617 \text{ \AA}$ ^{40,41} (pseudo-cubic unit cell of roughly 3.94 \AA).

X-ray reciprocal space maps (RSMs) of the three phases on different substrates in Fig. 2 show that the films are fully strained to the in-plane lattice parameter of the substrate. As expected, the out-of-plane lattice parameter of Sr_2IrO_4 expands (shrinks) relative to that of bulk under in-plane compressive (tensile) strain induced

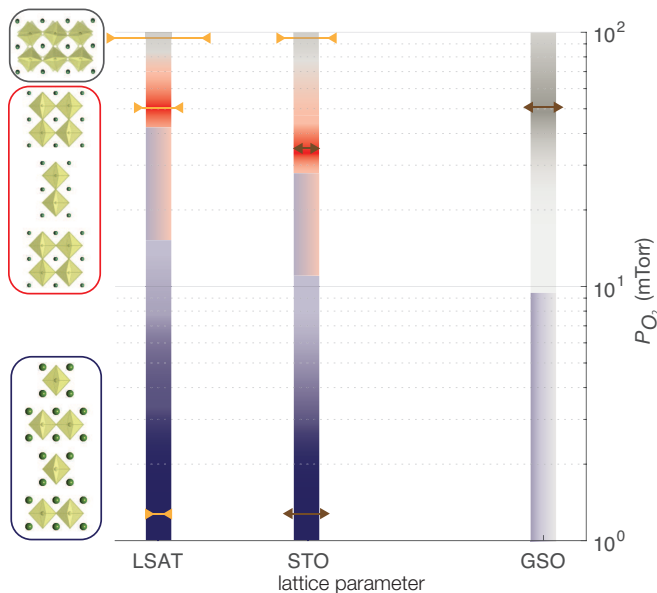


FIG. 4. Combined effect of epitaxial strain and background oxygen pressure. Stabilization of Sr_2IrO_4 , $\text{Sr}_3\text{Ir}_2\text{O}_7$ and SrIrO_3 films grown from a single $\text{Sr}_3\text{Ir}_2\text{O}_7$ target at a substrate temperature of 800°C . Vertical bars in blue, red and grey indicate the range of oxygen pressure at which the $n=1$, $n=2$, and $n=\infty$ phases, respectively, grow (higher opacity denotes higher crystalline quality of the stabilized phase). The images on the left are the crystal structures of these phases. Compressive (tensile) strain induced by the substrate on each structure is depicted by yellow (brown) arrows whose lengths are proportional to the magnitude of strain. We were not able to grow high quality Sr_2IrO_4 at low oxygen pressure on GSO substrates at these growth conditions (see Supplementary Information, Fig. S6³⁵).

by LSAT (STO) substrate. It decreases from 25.86 ± 0.05 Å on LSAT to 25.72 ± 0.03 Å on STO (tensile strain of $\approx +0.64\%$). Likewise, in-plane tensile (compressive) strain also results in a contraction (expansion) along the out-of-plane direction in $\text{Sr}_3\text{Ir}_2\text{O}_7$. It shrinks along the c -axis from 21.03 ± 0.03 Å under compressive strain on LSAT to 20.81 ± 0.04 Å under tensile strain on STO. These values are in good agreement with values for the bulk of $n=1$ and $n=2$ RP phases.^{38,42}

Further insight into the microstructure and composition of the films is provided by Transmission Electron Microscopy (TEM) on cross-section lamellas (Fig. 3). In agreement with the RSM results, we find that the films are fully strained on the substrate. The analysis of the electron diffraction patterns (Fig. S4³⁵) reveals in-plane orientation relationships for Sr_2IrO_4 and $\text{Sr}_3\text{Ir}_2\text{O}_7$ films where the unit cell of the iridate grows 45° rotated relative to the LSAT unit cell (Fig. 3(a, b)). On the other hand, orthorhombic SrIrO_3 (b as long axis) shows an epitaxial relationship of $(10\bar{1})_{\text{or}}[101]_{\text{or}}\text{SrIrO}_3 \parallel (001)[100]_{\text{LSAT}}$ (Fig. 3(c)).

Fig. 4 summarizes the entanglement of epitaxial strain and background oxygen pressure in the stabilization of

$\text{Sr}_{n+1}\text{Ir}_n\text{O}_{3n+1}$ phases. For example, Sr_2IrO_4 grows with excellent structural quality on LSAT (small lattice mismatch $\approx -0.26\%$) at oxygen pressure about 1 mTorr. However, this phase does not stabilize under a strain of $\approx +2\%$ (GSO substrate) over the range of oxygen pressures studied in this work. In this regard, Fig. S6³⁵ compares θ - 2θ scans of films grown on STO or GSO substrates at 800°C , and 1 mTorr or 10 mTorr. Sr_2IrO_4 epitaxial films of high structural quality are obtained on STO substrates while films of poor quality are grown on GSO under these conditions (this figure displays results from both Sr_2IrO_4 and $\text{Sr}_3\text{Ir}_2\text{O}_7$ targets). Furthermore, we obtain single-phase $\text{Sr}_3\text{Ir}_2\text{O}_7$ films at 50 mTorr on LSAT (lattice mismatch of $\approx -0.75\%$); and, at 35 mTorr on STO (lattice mismatch $\approx +0.15\%$, Fig. S1³⁵). Moreover, SrIrO_3 grows with outstanding structural quality tensile-strained ($\approx +0.51\%$) on GSO already above ≈ 40 mTorr (see also Supplementary Information, Fig. S2³⁵).

EDS analyses of the films show that the Sr/Ir ratio varies from 1.91, through 1.74, down to 1.12 for films grown under oxygen pressure ranging from 1 mTorr to 100 mTorr. These results are consistent with the thermodynamics trend pointed out by Nishio *et al.*, although they used a SrIrO_3 target:³⁶ reduced (increased) oxygen partial pressure assists the formation of $\text{Sr}_{n+1}\text{Ir}_n\text{O}_{3n+1}$ phases with lower (higher) n dimension. Nevertheless, the significant role they attribute to volatile IrO_3 in the chemical equilibrium equations they propose to explain their results do not work for our experiments where the substrate temperature do not go over 800°C .

An interpretation for our results could be based on PLD plume dynamics. In a simple kinetic model, the plume species are expected to diffuse while interacting with the background gas until reaching the substrate. Given the large difference in size and mass between Ir and Sr, it is expected that background oxygen pressure will significantly affect propagation velocity and angular distribution of Ir and Sr species which, in turn, will impact on the Sr/Ir cation ratio of the films.

At the working laser fluence of ≈ 1 J/cm², we observe that Sr is preferentially ablated from the target, as proved by Energy Dispersive Spectroscopy (EDS) analysis. In our experiments, following a series of 5000 shots, EDS results show a decrease of $\approx 15\%$ in the Sr/Ir ratio relative to the estimate of the original composition by the same method, providing evidence of that preferential ablation of Sr. The original stoichiometric Sr/Ir ratio is recovered after careful polishing of the surface of the target. This preferential ablation of Sr from the target leads to an Ir-rich target surface. We grew the films after a long preablation of the target surface to ensure that a steady state had been reached. Such a preferential ablation of Sr has previously been reported for a SrIrO_3 target at laser fluences varying from 0.4 to 2.0 J/cm².⁴³

At low background oxygen pressure, it is predicted that lighter Sr species outnumber heavier Ir species at the plume front.²⁸ This effect helps overcoming the Ir enrichment of the target surface owing to Sr preferential

ablation. As a result, films with Sr/Ir ratio higher than that of the $\text{Sr}_3\text{Ir}_2\text{O}_7$ polycrystalline target are grown at oxygen pressure around 1 mTorr on LSAT and STO substrates. Indeed, our results of complementary growths carried out from a target with a different Sr/Ir ratio hint that preferential ablation of Sr is likely not a key condition for the stabilization of the Sr_2IrO_4 phase at low oxygen pressure when a $\text{Sr}_3\text{Ir}_2\text{O}_7$ target is used (see Fig. S5³⁵). Then, as the oxygen pressure inside the chamber increases, the propagation behaviour of the species changes.²⁹ In this case, lighter and larger species, such as Sr, are preferentially scattered during their flight towards the substrate. Therefore, as the number of scattering events increases at high oxygen pressure, there is an enrichment in Ir along the direction normal to the substrate that leads to films with Sr/Ir ratio lower than that of the $\text{Sr}_3\text{Ir}_2\text{O}_7$ target.

This behaviour is consistent with the critical role of oxygen partial pressure in the stabilization of $\text{Sr}_{n+1}\text{Ir}_n\text{O}_{3n+1}$ phases put forward by Liu *et al.*, although they used a Sr_2IrO_4 target and set a laser fluence of 2 J/cm² to eliminate the possibility of preferential ablation of Sr.³⁷

On the other hand, kinetic models overlook the dependence of surface diffusion of species at the substrate surface on epitaxial strain. Indeed, in the framework of the model described above we expect that the cation ratio of species arriving at the substrate will determine the RP phase that can stabilize as a film, although strain can certainly hinder its stabilization. In contrast, we observe that epitaxial strain can promote the stabilization of different phases in films grown on different substrates under identical growth conditions of laser fluence, substrate temperature, and oxygen pressure.

Noteworthy, $\text{Sr}_3\text{Ir}_2\text{O}_7$ and SrIrO_3 phases are both grown in the same batch on LSAT and GSO substrates, respectively, under 50 mTorr of oxygen pressure from a $\text{Sr}_3\text{Ir}_2\text{O}_7$ target, as shown in the uppermost panels of Fig. 1. To further illustrate this, Fig. S7³⁵ demonstrates that SrIrO_3 and Sr_2IrO_4 phases stabilize on GSO and STO substrates, respectively, in films deposited from a Sr_2IrO_4 target in the same batch at 700 °C and 1 mTorr. All of the above suggests that the underlying mechanism behind the arrangement of SrO and IrO₂ layers at atomic scale during growth is highly dependent on strain. We hypothesize that tensile strain decreases surface diffusion and mobility of adatoms, thus hindering the growth of Sr_2IrO_4 and $\text{Sr}_3\text{Ir}_2\text{O}_7$ phases on GSO substrates at low oxygen pressures. This hypothesis is in agreement with the report of a non-negligible barrier for adatom transport at low pressure brought about by tensile epitaxial strain during the growth of complex oxides by PLD.³⁰ It is worth bearing in mind that SrIrO_3 has lower lattice mismatch with GSO, $\approx +0.51\%$, than Sr_2IrO_4 ($\approx +2\%$) or $\text{Sr}_3\text{Ir}_2\text{O}_7$ ($\approx +1.6\%$), providing the driving force for stabilization of SrIrO_3 when growth conditions are thermodynamically suited to the stabilization of that phase, *i.e.* at low substrate temperature or high oxygen pressure.

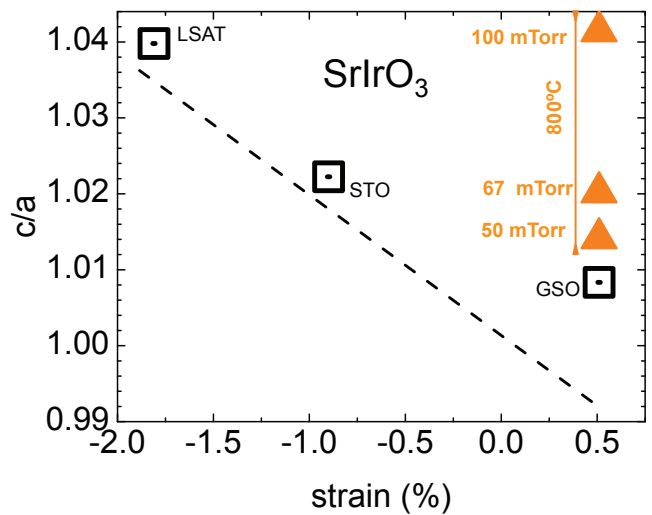


FIG. 5. Variation of the c/a ratio of pseudocubic lattice parameters with strain (open squares) and background oxygen pressure (solid triangles) of SrIrO_3 films. The open squares correspond to samples synthesized at 67 mTorr and 700 °C in the same batch. The triangles correspond to samples deposited on GSO at 800 °C, under different oxygen pressures (this data are extracted from XRD θ - 2θ scans shown in Fig. S2 and Fig. S8³⁵). The dotted line corresponds to c/a calculated for a Poisson's ratio of $\nu=0.3$.

We now explore the deformation of the unit cell of SrIrO_3 as function of strain for samples synthesized under different temperatures and oxygen pressures. The values shown in Fig. 5 are in accordance with literature.^{13,43,44} Under the optimized growth conditions (700 °C, 67 mTorr), the tetragonal distortion, c/a , decreases with tensile strain, although at a lower rate than expected assuming a Poisson's ratio^{45,46} $\nu = 0.3$, a value common to other oxide-perovskites (see dashed line in Fig. 5). On the other hand, the c/a ratio increases with increasing temperature (oxygen pressure) while keeping the oxygen pressure (temperature) constant. For instance, the film grown at the highest pressure (100 mTorr) exhibits the highest c/a ratio (Fig. 5). Thus, we exclude the presence of oxygen vacancies as the cause of the deformation of the unit cell of SrIrO_3 depicted in Fig. 5.^{47,48} The behaviour of c/a instead presumably stems from an increase of cation vacancies with increasing temperature and/or oxygen pressure. Indeed, the preferential scattering of Sr in the plume at high oxygen pressure predicted by the kinetic model described above would result in SrIrO_3 films with an increased concentration of Sr vacancies. This prediction is consistent with the cell expansion observed in Fig. 5 for the films grown under tensile strain.

Non-stoichiometric Sr/Ir ratio in SrIrO_3 films may affect their electrical properties. Fig. 6 shows the temperature dependence of resistivity of SrIrO_3 films grown at 800 °C and oxygen pressure from 35 mTorr to 100 mTorr. Films grown at the end values over this window pressure

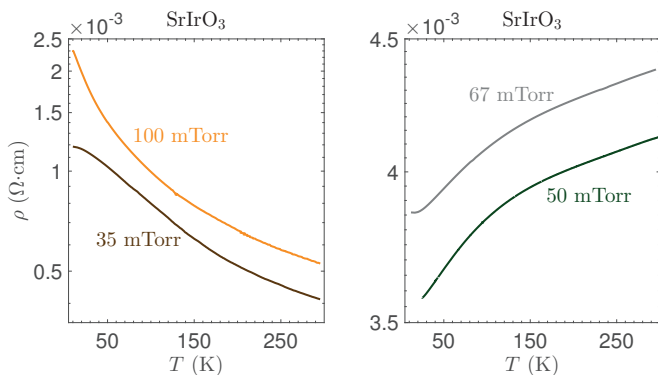


FIG. 6. Electrical resistivity, $\rho(T)$, of SrIrO₃ on GSO epitaxial films grown at varying oxygen pressures and 800°C. See supplementary Information for XRD θ - 2θ scans of films (Fig. S2³⁵).

show semiconducting behaviour (left panel), while those grown at intermediate values exhibit metallic character (right panel). The lower crystalline quality of the film grown at 35 mTorr (compared to that of films grown at higher pressure, Fig. S2³⁵) and the increase of cation vacancies postulated above in the film grown at 100 mTorr can be associated with the semiconducting behaviour of SrIrO₃ displayed in the left panel of Fig. 6. This proposed picture of semiconducting electrical behaviour arising from Sr vacancies is in good agreement with the metallic behaviour of SrIrO₃ films grown at the highest oxygen pressure, 100 mTorr, from a Sr₂IrO₄ target, Fig. S9.³⁵ Given that the stabilization of layered RP phases do not require overall stoichiometric growth conditions, the content of Sr vacancies in SrIrO₃ films grown at high pressure is expected to be lower when using a Sr₂IrO₄ target compared to a Sr₃Ir₂O₇ target, provided that growth conditions keep unchanged. The reduced concentration of cation vacancies results in a metallic behaviour in the former case as shown in Fig. S9.³⁵

We now discuss the effect of oxygen pressure during growth and substrate induced strain on the temperature dependent magnetization of Sr₂IrO₄ (Fig. 7). As the canting of Ir magnetic moments in Sr₂IrO₄ follow the IrO₆ octahedral rotations,^{49–51} epitaxial strain is expected to have a strong influence on its magnetic properties. We observe a sharp magnetic transition around $T \approx 240$ K (bulk value⁵) for the film grown compressively strained on LSAT at the lowest oxygen pressure, 1 mTorr. This transition is flattened in the film grown on LSAT at 10 mTorr, resulting from a decreased structural quality of the films grown at higher pressures. Indeed, we found an increase of around 20% in the FWHM of the (00 $\underline{12}$) XRD peak with an increase of oxygen pressure from 1 mTorr to 10 mTorr, while no significant difference was found in the out-of-plane lattice parameter between both films (25.86±0.05 Å and 25.85±0.06 Å, respectively). We also find that the ferromagnetic component, which stems from the canted antiferromagnetic order, is lower in the film grown on STO (ten-

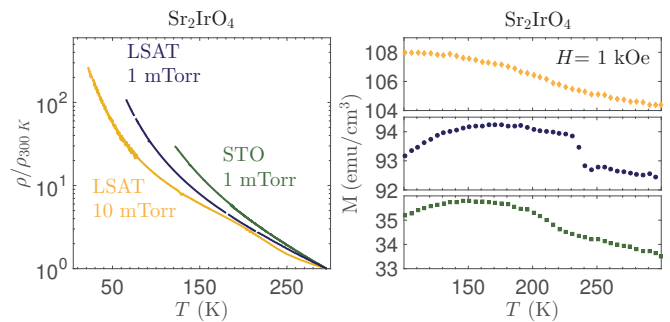


FIG. 7. Left panel: temperature dependence of electrical resistivity, $\rho(T)$, normalized to room temperature of Sr₂IrO₄ films grown at 800°C on LSAT at 1 mTorr (blue), LSAT at 10 mTorr (yellow), and STO at 1 mTorr (green). Right panel: temperature dependence of magnetization, $M(T)$, at $H = 1$ kOe of the same films.

sile strain) than in those grown on LSAT (compressive strain). This is in accordance with previous studies on 200 nm-thick Sr₂IrO₄ films where higher tensile strain was reported to lead to lower octahedral rotation, resulting in a weaker ferromagnetic component.⁵² Electrical resistivity does not show any sensitivity to the magnetic transition, as reported for single crystals.^{53,54}

The temperature dependence of resistivity, $\rho(T)$, and Seebeck coefficient, $S(T)$, of Sr₂IrO₄, Sr₃Ir₂O₇, and SrIrO₃ on LSAT are shown in Fig. 8. Epitaxial compression on LSAT increases with increasing dimensionality of the material, n . Electrical transport of these phases is consistent with the widely accepted bandwidth-driven insulator-to-metal transition previously reported on the Sr _{$n+1$} Ir _{n} O_{3 $n+1$} series as a result of increasing dimensionality, n : Sr₂IrO₄/LSAT(001) shows semiconducting behavior and high resistivity; Sr₃Ir₂O₇/LSAT(001) exhibits a semiconducting-like behavior over the whole range of temperature with a characteristic feature that reflects the antiferromagnetic transition expected at $T = 285$ K in bulk;⁵⁵ and, SrIrO₃/LSAT(001) presents a very low resistivity and metallic behavior, with a slight upturn at low temperatures.

The Seebeck coefficient of the films on LSAT is positive in the whole range of temperatures measured, Fig. 8. The magnitude of $S(T)$ in Sr₂IrO₄ is in accordance with previous reports on polycrystalline^{21,56} and single-crystal samples.^{53,54} We observed a clear plateau below ≈ 200 K for the epitaxial films that could be linked to the canted antiferromagnetic structure reported in bulk,^{5,49} although no anomaly of the Seebeck coefficient at the magnetic transition temperature has been observed in single crystals^{53,54} or polycrystalline^{21,56} Sr₂IrO₄. As expected, the value of $S(T)$ is much lower in Sr₃Ir₂O₇ and SrIrO₃ than in Sr₂IrO₄, due to their higher electrical conductivity. The $n=2$ phase shows a maximum around ≈ 200 K, which does not seem to correlate with the magnetic transition, and may be related to electron phonon-scattering. The significant role of phonon-assisted charge excitation across the Mott gap in Sr₃Ir₂O₇

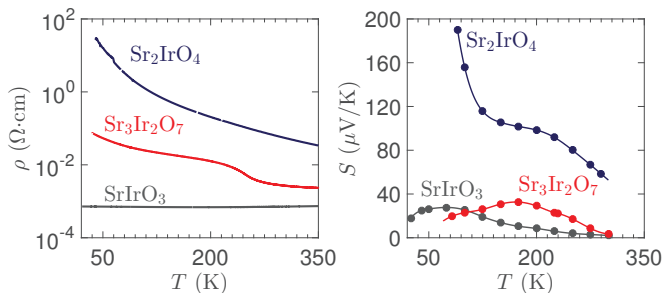


FIG. 8. Temperature dependence of the electrical resistivity, $\rho(T)$, and Seebeck coefficient, $S(T)$, of Sr_2IrO_4 , $\text{Sr}_3\text{Ir}_2\text{O}_7$, and SrIrO_3 films grown on LSAT(001). The lines in the Seebeck figure are a guide to the eye.

has been reported.⁵⁷ A similar feature is observed at ≈ 50 K for SrIrO_3 , a paramagnetic material with no magnetic transition reported.^{58,59} We are not aware of any other measurements of the thermoelectrical properties of epitaxial films of Sr_2IrO_4 or $\text{Sr}_3\text{Ir}_2\text{O}_7$.

The effect of epitaxial strain on the thermoelectric properties of SrIrO_3 is shown in Fig. 9. Values of the Seebeck coefficient, in the range 10–20 $\mu\text{V}/\text{K}$, for the film grown on STO are in agreement with those recently reported for 8 nm-thick $\text{SrIrO}_3/\text{STO}$ films.⁶⁰ Differences between our data and those reported therein may be due to thickness disparity between the films investigated. Our films are prepared in the same batch. Thus, the dissimilarity in their electronic properties must stem from different substrate induced strain: -1.8% , -0.9% and $+0.5\%$ for LSAT, STO and GSO, respectively. Moreover, electrical transport measurements were carried out immediately after growth for three days in a row hence, degradation effects reported to occur in the SrIrO_3 films⁴³ are expected to be negligible. The temperature dependence of $\rho(T)$ shows metallic behavior at high temperature, with a crossover towards a thermally activated state defined by $(d\rho(T)/dT) < 0$ at low temperature in the samples under compressive strain. The magnitude of the $\rho(T)$ and the value of the crossover temperature do not follow any clear dependence with the c/a ratio. Therefore, they cannot be directly related to a change in bandwidth with strain.

This is in contrast to previous studies about the strain effect on electrical transport in SrIrO_3 films.^{13,61} These studies are consistent with a bandwidth controlled via strain model, according to which the Ir–O–Ir angle decreases (increases) by compressive (tensile) strain (while Ir–O length is not modified), thus shrinking (expanding) the bandwidth. Such scenario echoes the behavior observed in Sr_2IrO_4 ,¹² but essential differences between Sr_2IrO_4 and SrIrO_3 have been pointed out. In particular, SrIrO_3 exhibits out-of-plane octahedral rotations along the [110] pseudocubic direction, but no such [110] rotations are found experimentally in Sr_2IrO_4 .⁴⁴ Furthermore, a reported narrower bandwidth in SrIrO_3 than in Sr_2IrO_4 casts doubt on the conventional picture of in-

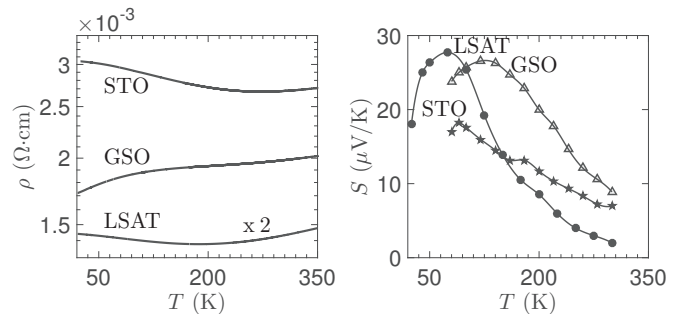


FIG. 9. Temperature dependence of the electrical resistivity, $\rho(T)$, and Seebeck coefficient, $S(T)$, of SrIrO_3 films grown on GSO (Δ), STO ($*$) and LSAT (\circ). These films were grown in the same batch (1 mTorr, 700°C). The resistivity of the film grown on LSAT has a scale factor of 2. The lines in the Seebeck figure are a guide to the eye. (See Fig. S8³⁵ for XRD measurements of the films).

creased bandwidth with increasing dimensionality, n , in the RP series of iridates.⁴⁴ On the other hand, the Seebeck coefficients are very similar for all SrIrO_3 films, with only a slight dependence on epitaxial strain, Fig. 9. As thermoelectric voltage is measured in open circuit conditions, no electrical current flows through the sample, and consequently $S(T)$ is not so sensitive to grain boundaries and point-defect scattering as it is electrical resistivity. Indeed, $S(T)$ rather depends on the intrinsic electronic structure of the conductor. Therefore, we suggest that localization induced by disorder is responsible for the temperature dependence of the resistivity observed in these films. This is in agreement with previous observations of a persistent Drude-like peak in the optical conductivity of SrIrO_3 films under comparable strain.¹³

III. CONCLUSIONS

Our results reveal an intricate coupling between epitaxial strain and oxygen pressure during PLD growth of $\text{Sr}_{n+1}\text{Ir}_n\text{O}_{3n+1}$ films. Such coupling suggests the possibility of growing artificial superlattices of iridates with tailored electronic and magnetic properties by varying the background pressure during deposition.^{62,63} In addition, future works could address atomic-scale effects of strain on the surface diffusion of species during growth, and the influence of the oxidation state of the arriving species to promote the stabilization of RP phases with different cation stoichiometry.^{23,24,30,64} This study would require *in-situ* characterization to monitor the film growth, and would provide fundamental insights into the growth process that may lead to the stabilization of new phases of layered materials. We have also shown that weak localization effects owing to accommodation to compressive epitaxial strain dominate the conductivity of the metallic SrIrO_3 films, beyond the simple model of bandwidth controlled via strain.

ACKNOWLEDGMENTS

This work has received financial support from Ministerio de Economía y Competitividad (Spain) under project No. MAT2016–80762–R, Xunta de Galicia (Centro singular de investigación de Galicia accreditation 2016–

2019, ED431G/09) and the European Union (European Regional Development Fund–ERDF).

A.G.L. acknowledges financial support from Universidad de Santiago de Compostela. L.I. also acknowledges Mineco–Spain for support under a FPI grant.

* araceli.gutierrez@urjc.es

- ¹ J. B. Goodenough, Magnetism and the Chemical Bond (John Wiley and Sons, New York, 1963).
- ² M. Imada, A. Fujimori, and Y. Tokura, *Reviews of Modern Physics* **70** (1998), 10.1103/RevModPhys.70.1039.
- ³ Y. Tokura and N. Nagaosa, *Science* **288** (2000), 10.1126/science.288.5465.462.
- ⁴ B. J. Kim, H. Jin, S. J. Moon, J. Y. Kim, B. G. Park, C. S. Leem, J. Yu, T. W. Noh, C. Kim, S. J. Oh, J. H. Park, V. Durairaj, G. Cao, and E. Rotenberg, *Physical Review Letters* **101** (2008), 10.1103/PhysRevLett.101.076402.
- ⁵ B. J. Kim, H. Ohsumi, T. Komesu, S. Sakai, T. Morita, H. Takagi, and T. Arima, *Science* **323** (2009), 10.1126/science.1167106.
- ⁶ J. L. Lado and V. Pardo, *Physical Review B* **92** (2015), 10.1103/PhysRevB.92.155151.
- ⁷ Z. T. Liu, M. Y. Li, Q. F. Li, J. S. Liu, W. Li, H. F. Yang, Q. Yao, C. C. Fan, X. G. Wan, Z. Wang, and D. W. Shen, *Scientific Reports* (2016), 10.1038/srep30309.
- ⁸ Y. Okada, D. Walkup, H. Lin, C. Dhital, T. R. Chang, S. Khadka, W. W. Zhou, H. T. Jeng, M. Paranjape, A. Bansil, Z. Q. Wang, S. D. Wilson, and V. Madhavan, *Nature Materials* **12** (2013), 10.1038/nmat3653.
- ⁹ Q. Wang, Y. Cao, J. A. Waugh, S. R. Park, T. F. Qi, G. C. O. B. Korneta, and D. S. Dessau, *Physical Review B* **87** (2013), 10.1103/PhysRevB.87.245109.
- ¹⁰ B. M. Wojek, M. H. Berntsen, S. Boseggia, A. T. Boothroyd, D. Prabhakaran, D. F. McMorrow, H. M. Rnnow, J. Chang, and O. Tjernberg, *Journal of Physics: Condensed Matter* **24** (2012), 10.1088/0953-884/24/44/445602A.
- ¹¹ J. Nichols, J. Terzic, E. G. Bittle, O. B. Korneta, L. E. D. Long, J. W. Brill, G. Cao, and S. S. A. Seo, *Applied Physics Letters* **102** (2013), 10.1063/1.4801877.
- ¹² C. Rayan Serrao, J. Liu, J. T. Heron, G. Singh-Bhalla, A. Yadav, S. J. Suresha, R. J. Paull, D. Yi, J.-H. Chu, M. Trassin, A. Vishwanath, E. Arenholz, C. Frontera, J. Železný, T. Jungwirth, X. Marti, and R. Ramesh, *Physical Review B* **87** (2013), 10.1103/PhysRevB.87.085121.
- ¹³ J. H. Gruenewald, J. Nichols, J. Terzic, G. Cao, J. W. Brill, and S. S. A. Seo, *Journal of Materials Research* **29** (2014), 10.1557/jmr.2014.288.
- ¹⁴ S. J. Moon, H. Jin, K. W. Kim, W. S. Choi, Y. S. Lee, J. Yu, G. Cao, A. Sumi, H. Funakubo, C. Bernhard, and T. W. Noh, *Physical Review Letters* **101** (2008), 10.1103/PhysRevLett.101.226402.
- ¹⁵ C. Wang, H. Seinige, G. Cao, J.-S. Zhou, J. B. Goodenough, and M. Tsoi, *Physical Review X* **4** (2014), 10.1103/PhysRevX.4.041034.
- ¹⁶ I. Fina, X. Marti, D. Yi, J. Liu, J. Chu, C. Rayan-Serrao, S. Suresha, A. Shick, J. Zelezny, T. Jungwirth, J. Fontcuberta, and R. Ramesh, *Nature Communications* **5** (2014), 10.1038/ncomms5671.
- ¹⁷ C. Wang, H. Seinige, G. Cao, J.-S. Zhou, J. B. Goodenough, and M. Tsoi, *Journal of Applied Physics* **117** (2015), 10.1063/1.4913300.
- ¹⁸ C. Wang, H. Seinige, G. Cao, J. S. Zhou, J. B. Goodenough, and M. Tsoi, *Physical Review B* **92** (2015), 10.1103/PhysRevB.92.115136.
- ¹⁹ H. Seinige, M. Williamson, S. Shen, C. Wang, G. Cao, J. Zhou, J. B. Goodenough, and M. Tsoi, *Physical Review B* **94** (2016), 10.1103/PhysRevB.94.214434.
- ²⁰ M. Williamson, S. Shen, G. Cao, J. Zhou, J. B. Goodenough, and M. Tsoi, *Physical Review B* **97** (2018), 10.1103/PhysRevB.97.134431.
- ²¹ I. Pallecchi, M. T. Buscaglia, V. Buscaglia, E. Gilioli, G. Lamura, F. Telesio, M. R. Cimberle, and D. Marre, *Journal of Physics–Condensed Matter* **28** (2016), 10.1088/0953-8984/28/10/105502.
- ²² S. S. A. Seo, J. Nichols, J. Hwang, J. Terzic, J. H. Gruenewald, M. Souris, J. Thompson, J. G. Connell, and G. Cao, *Applied Physics Letters* **109** (2016), 10.1063/1.4967450.
- ²³ J. H. Lee, G. Luo, I. C. Tung, S. H. Chang, Z. Luo, M. Malshe, M. Gadre, A. Bhattacharya, S. M. Nakhmanson, J. A. Eastman, H. Hong, J. Jellinek, D. Morgan, D. D. Fong, and J. Freeland, *Nature Materials* **13** (2014), 10.1038/nmat4039.
- ²⁴ Y. F. Nie, Y. Zhu, C. H. Lee, L. F. Kourkoutis, J. A. Mundy, J. Junquera, P. Ghosez, D. J. Baek, S. Sung, X. X. Xi, K. M. Shen, D. A. Muller, and D. G. Schlom, *Nature Communications* **5** (2014), 10.1038/ncomms5530.
- ²⁵ S. Wicklein, A. Sambri, S. Amoruso, X. Wang, A. Koehl, and R. Dittmann, *Applied Physics Letters* **101** (2012), 10.1063/1.4754112.
- ²⁶ H. Schraknepper, C. Baumer, F. Gunkel, R. Dittmann, and R. A. D. Souza, *APL Materials* **4** (2016), 10.1063/1.4972996.
- ²⁷ D. M. Packwood, S. Shiraki, and T. Hitosugi, *Physical Review Letters* **111** (2013), 10.1103/PhysRevLett.111.036101.
- ²⁸ A. Sambri, C. Aruta, E. D. Gennaro, X. Wang, U. S. di Uccio, F. M. Granozio, and S. Amoruso, *Journal of Applied Physics* **119** (2016), 10.1063/1.4943589.
- ²⁹ R. Groenen, J. Smit, K. Orsel, A. Vailionis, B. Bastiaens, M. Huijben, K. Boller, G. Rijnders, and G. Koster, *APL Materials* **3** (2015), 10.1063/1.4926933.
- ³⁰ A. Tselev, R. K. Vasudevan, A. G. Gianfrancesco, L. Qiao, T. L. Meyer, H. N. Lee, M. D. Bielecki, A. P. Baddorf, and S. V. Kalinin, *Crystal Growth and Design* **16** (2016), 10.1021/acs.cgd.5b01826.
- ³¹ H. Brune, K. Bromann, H. Rder, K. Kern, J. Jacobsen, P. Stoltze, K. Jacobsen, and J. Norkov, *Physical Review B* **52** (1995), 10.1103/PhysRevB.52.R14380.
- ³² M. Schroeder and D. E. Wolf, *Surface Science* **375** (1997), 10.1016/S0039-6028(96)01250-2.
- ³³ C. Xu, S. Wicklein, A. Sambri, S. Amoruso, M. Moors, and R. Dittmann,

- J. Phys. D: Appl. Phys. **47** (2014), 10.1088/0022-3727/47/3/054009.
- ³⁴ S. Pandya, A. R. Damodaran, R. Xu, S. L. Hsu, J. C. Agar, and L. W. Martin, *Scientific Reports* **26075** (2016), 10.1038/srep26075.
- ³⁵ See supplementary material for detailed experimental description and additional figures.
- ³⁶ K. Nishio, H. Y. Hwang, and Y. Hikita, *APL Materials* **4** (2016), 10.1063/1.4943519.
- ³⁷ X. Liu, Y. Cao, B. Pal, S. Middey, M. Kareev, Y. Choi, P. Shafer, D. Haskel, E. Arenholz, and J. Chakhalian, *Physical Review Materials* **1** (2017), 10.1103/PhysRevMaterials.1.075004.
- ³⁸ Q. Huang, J. L. Soubeyroux, O. Chmaissem, I. N. Sora, A. Santoro, R. J. Cava, J. J. Krajewski, and W. F. P. Jr, *Journal of Solid State Chemistry* **112** (1994), 10.1006/jssc.1994.116.
- ³⁹ T. Hogan, L. Bjaalie, L. Zhao, C. Belvin, X. Wang, C. G. V. de Walle, D. Hsieh, and S. D. Wilson, *Physical Review B* **93** (2016), 10.1103/PhysRevB.93.134110.
- ⁴⁰ J. G. Zhao, L. X. Yang, Y. Yu, F. Y. Li, R. C. Yu, Z. Fang, L. C. Chen, and C. Q. Jin, *Journal of Applied Physics* **103** (2008), 10.1063/1.2908879.
- ⁴¹ D. Puggioni and J. M. Rondinelli, *Journal of Applied Physics* **119** (2016), 10.1063/1.4942651.
- ⁴² M. A. Subramanian, M. K. Crawford, and R. L. Harlow, *Materials Research Bulletin* **29** (1994), 10.1016/0025-5408(94)90120-1.
- ⁴³ D. J. Groenendijk, N. Manca, G. Mattoni, L. Kootstra, S. Gariglio, Y. Huang, E. van Heumen, and A. D. Caviglia, *Applied Physics Letters* **109** (2016), 10.1063/1.4960101.
- ⁴⁴ Y. F. Nie, P. D. C. King, C. H. Kim, M. Uchida, H. I. Wei, B. D. Faeth, J. P. Ruff, L. Xie, X. Pan, C. Fennie, D. G. Schlom, and K. M. Shen, *Physical Review Letters* **114** (2015), 10.1103/PhysRevLett.114.064401.
- ⁴⁵ G. N. Greaves, A. L. Greer, R. S. Lakes, and T. Rouxel, *Nature Materials* **10** (2011), 10.1038/NMAT3134.
- ⁴⁶ C. Huang and L. Chen, *Advanced Materials* **28** (2016), 10.1002/adma.201601363.
- ⁴⁷ L. Iglesias, A. Sarantopoulos, C. Magen, and F. Rivadulla, *Physical Review B* **95** (2017), 10.1103/PhysRevB.95.165138.
- ⁴⁸ U. Aschauer, R. Pfenninger, S. M. Selbach, T. Grande, and N. A. Spaldin, *Physical Review B* **88** (2013), 10.1103/PhysRevB.88.054111.
- ⁴⁹ S. Boseggia, H. C. Walker, J. Vale, R. Springell, Z. Feng, R. S. Perry, M. M. Sala, S. P. C. H. M. Ronnow, and D. F. McMorrow, *Journal of Physics: Condensed Matter* **25** (2013), 10.1088/0953-8984/25/12/122202.
- ⁵⁰ M. Ge, T. F. Qi, O. B. Korneta, D. E. D. Long, P. Schlottmann, W. P. Crummett, , and G. Cao, *Physical Review B* **84** (2011), 10.1103/PhysRevB.84.100402.
- ⁵¹ F. Ye, S. Chi, B. C. Chakoumakos, J. A. Fernandez-Baca, T. Qi, and G. Cao, *Physical Review B* **87** (2013), 10.1103/PhysRevB.87.140406.
- ⁵² L. Miao, H. Xu, and Z. Q. Mao, *Physical Review B* **89** (2014), 10.1103/PhysRevB.89.035109.
- ⁵³ S. Chikara, O. Korneta, W. P. Crummett, L. E. DeLong, P. Schlottmann, and G. Cao, *Journal of Applied Physics* **107** (2010), 10.1063/1.3362912.
- ⁵⁴ T. Shimura, Y. Inaguma, T. Nakamura, M. Itoh, and Y. Morii, *Physical Review B* **52** (1995), 10.1103/PhysRevB.52.9143.
- ⁵⁵ G. Cao, Y. Xin, C. S. Alexander, J. E. Crow, P. Schlottmann, M. K. Crawford, R. Harlow, and W. Marshall, *Physical Review B* **66** (2002), 10.1103/PhysRevB.66.214412.
- ⁵⁶ N. S. Kini, A. M. Strydom, H. S. Jeevan, C. Geibel, , and S. Ramakrishnan, *Journal of Physics: Condensed Matter* **18**, 8205 (2006).
- ⁵⁷ H. J. Park, C. H. Sohn, D. W. Jeong, G. Cao, K. W. Kim, S. J. Moon, H. Jin, D. Y. Cho, and T. W. Noh, *Physical Review B* **89** (2014), 10.1103/PhysRevB.89.155115.
- ⁵⁸ G. Cao, V. Durairaj, S. Chikara, L. E. DeLong, S. Parkin, and P. Schlottmann, *Physical Review B* **76** (2007), 10.1103/PhysRevB.76.100402.
- ⁵⁹ J. Fujioka, T. Okawa, A. Yamamoto, and Y. Tokura, *Physical Review B* **95** (2017), 10.1103/PhysRevB.95.121102.
- ⁶⁰ N. Manca, D. J. Groenendijk, I. Pallecchi, C. Auricchio, L. M. K. Tang, F. Telesio, G. Mattoni, A. McCollam, S. Picozzi, and A. D. Caviglia, *Physical Review B* **97** (2018), 10.1103/PhysRevB.97.081105.
- ⁶¹ A. Biswas, K. S. Kim, and Y. H. Jeong, *Journal of Applied Physics* **116** (2014), 10.1063/1.4903314.
- ⁶² J. Matsuno, K. Ihara, S. Yamamura, H. Wadati, K. Ishii, V. V. Shankar, H. Y. Kee, and H. Takagi, *Physical Review Letters* **114** (2015), 10.1103/PhysRevLett.114.247209.
- ⁶³ Y. Ohuchi, J. Matsuno, N. Ogawa, Y. Kozuka, M. Uchida, Y. Tokura, and M. Kawasaki, *Nature Communications* **9** (2018), 10.1038/s41467-017-02629-3.
- ⁶⁴ A. Tselev, R. K. Vasudevan, A. G. Gianfrancesco, L. Qiao, P. Ganesh, T. L. Meyer, H. N. Lee, and A. P. Baddorf, and S. V. Kalinin, *ACS Nano* **9** (2015), 10.1021/acsnano.5b00743.